ADVANCED MATERIALS
www.advmat.de

Reducing Gases Triggered Cathode Surface Reconstruction for Stable Cathode–Electrolyte Interface in Practical All-Solid-State Lithium Batteries

Bingkai Zhang, Zhiwei He, Tiefeng Liu, Zeheng Li, Shaojian Zhang, Wenguang Zhao, Zu-Wei Yin, Zengqing Zhuo, Mingjian Zhang, Feng Pan, Shanqing Zhang, Zhan Lin,* and Jun Lu**

The interfacial compatibility between cathodes and sulfide solid-electrolytes (SEs) is a critical limiting factor of electrochemical performance in all-solid-state lithium-ion batteries (ASSLBs). This work presents a gas–solid interface reduction reaction (GSIRR), aiming to mitigate the reactivity of surface oxygen by inducing a surface reconstruction layer (SRL) . The application of a SRL, CoO/Li_2CO_3, onto $LiCoO_2$ (LCO) cathode results in impressive outcomes, including high capacity (149.7 mAh g^{-1}), remarkable cyclability (retention of 84.63% over 400 cycles at 0.2 C), outstanding rate capability (86.1 mAh g^{-1} at 2 C), and exceptional stability in high-loading cathode (28.97 and 23.45 mg cm^{-2}) within ASSLBs. Furthermore, the SRL CoO/Li_2CO_3 enhances the interfacial stability between LCO and $Li_{10}GeP_2S_{12}$ as well as Li_3PS_4 SEs. Significantly, the experiments suggest that the GSIRR mechanism can be broadly applied, not only to LCO cathodes but also to $LiNi_{0.8}Co_{0.1}Mn_{0.1}O_2$ cathodes and other reducing gases such as H_2S and CO, indicating its practical universality. This study highlights the significant influence of the surface chemistry of the oxide cathode on interfacial compatibility, and introduces a surface reconstruction strategy based on the GSIRR process as a promising avenue for designing enhanced ASSLBs.

1. Introduction

Driven by the safety issue of traditional liquid lithium-ion batteries , researchers have incorporated inorganic solid-electrolytes (SEs) into lithium-ion batteries. This innovation has led to the advancement from liquid-based systems to all-solid-state lithium-ion batteries (ASSLBs).[1,2,3,4] Notably, sulfide SEs such as Li_6PS_5Cl (LPSCl),[5,6] $Li_{10}GeP_2S_{12}$ (LGPS),[5,7] and β-Li_3PS_4 (LPS)[8] have exhibited significant potential in ASSLBs because of high ionic conductivity and mechanically soft nature.[5,9,10] Despite these advantages, sulfide SEs possess limited electrochemical windows (<2.1 V versus Li/Li^+), and the compatibility between cathode active materials (CAM) and SEs (CAM–SE interface) remains challenging, leading to poor cycling performance of ASSLBs.[11–14] Furthermore, interphases tend to develop rapidly between oxide cathodes, particularly layered $LiTMO_2$ (TM = Co, Ni, Mn), $LiNi_{0.8}Co_{0.1}Mn_{0.1}O_2$ (NCM811), and sulfide SEs, further complicating matters and earing the designation of a "black box" in solid–solid interfacial chemistry.[14–16] Consequently, the integration of a thin interface layer that ensures stability between CAM and SE (depicted in Figure S1a, Supporting Information) has been proposed to address these challenges. Unfortunately, the procedure indeed aggrandizes the complexity of preparing technology with extra cost. Therefore, the pursuit of a stable and

B. Zhang, Z. He, S. Zhang, S. Zhang, Z. Lin
Guangdong Provincial Key Laboratory of Plant Resources Biorefinery
School of Chemical Engineering and Light Industry
Guangdong University of Technology
Guangzhou 510006, China
E-mail: zhanlin@gdut.edu.cn

B. Zhang, S. Zhang, Z. Lin
Jieyang Branch of Chemistry and Chemical Engineering
Guangdong Laboratory
Jieyang 515200, P. R. China

T. Liu, Z. Li, J. Lu
College of Chemical and Biological Engineering
Zhejiang University
Hangzhou 310058, China
E-mail: 11728048@zju.edu.cn; junlu@anl.gov

W. Zhao, Z.-W. Yin, F. Pan
School of Advanced Materials
Peking University
Shenzhen Graduate School, Shenzhen 518055, China

Z. Zhuo
Advanced Light Source
Lawrence Berkeley National Laboratory
Berkeley CA 94720, USA

M. Zhang
School of Science and Engineering
The Chinese University of Hong Kong
Shenzhen 518172, China

The ORCID identification number(s) for the author(s) of this article can be found under https://doi.org/10.1002/adma.202305748

DOI: 10.1002/adma.202305748

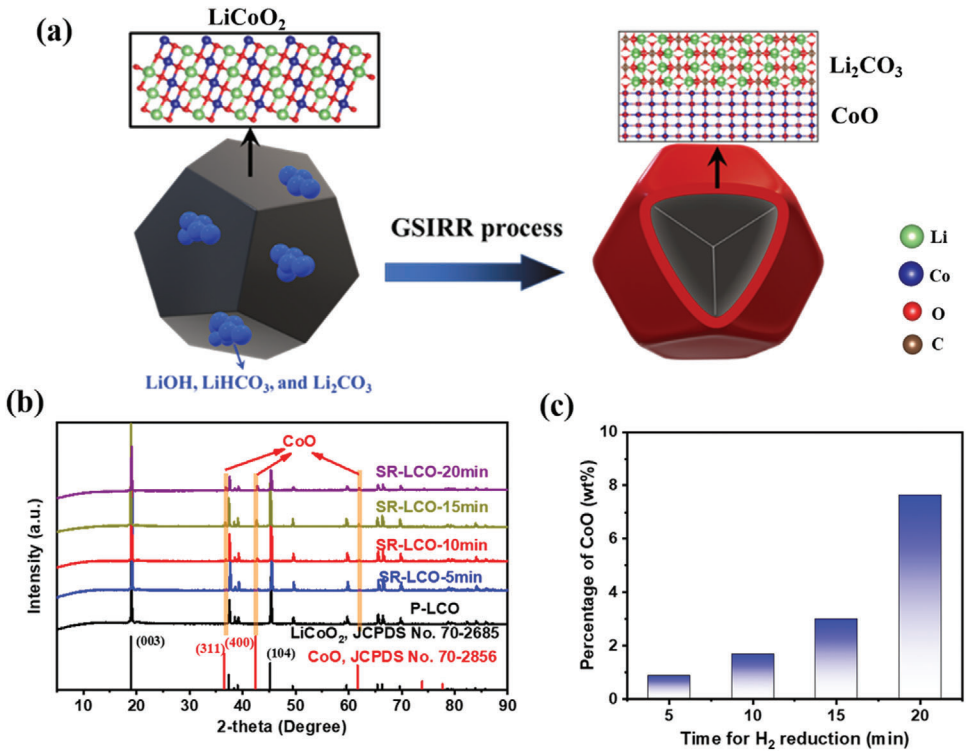

Figure 1. The formation and synthetic pathway of surface reconstruction layer LCO (SRL-LCO). a) Visual depiction of the gas–solid interface reduction reaction (GSIRR) mechanism. This diagram illustrates the GSIRR process wherein oxide cathodes react with a reducing gas to form a CoO/Li_2CO_3 layer on the particle's surface. b) X-ray diffraction (XRD) analysis of of LCO pre and post GSIRR process. c) Quantifying CoO content in SR-LCO: the weight percentage (wt%) of CoO within SR-LCO composite was obtained from XRD Rietveld refinement techniques.

compatible CAM/sulfide SEs interface through interfacial optimization without resorting the use of a thin interface layer (as illustrated in Figure S1b, Supporting Information), emerges as an exceedingly significant and formidable task in the realm of ASSLBs.[16]

Currently, typical acidic oxides such as Li_3PO_4,[17] $LiNbO_3$,[18] and $Li_4Ti_5O_{12}$[19] are employed to create an environment where lithium potential is the intermediate state between that of the oxide cathode and the sulfide SE and smoothing chemical potential difference at the interface. This arrangement helps in mitigating the chemical potential disparity at the interface. These oxides are applied as coatings onto cathode oxide materials using methods ranging from wet chemical techniques to advanced physical processes.[20,21] Nonetheless, achieving a uniform, dense, and intimate coating layer on the surface of active cathode material remains challenging. This challenge is further compounded by the interplay of two-phase interfacial energy, volumetric strain, and the development of cracks and delamination during repetitive cycling (refer to Figure S2a, Supporting Information). Moreover, the coating layer usually leads to a compromise in the active cathode loading, which makes them challenging to satisfy commercial areal capacity promotion (always >2.5 mAh cm^{-2}, Figure S3, Supporting Information). Herein, we turn our attention to "in situ phase transition induced coating," which can enhance the structural matching between cathode material and coating layer as well as improve their interfacial stability, and put forward a universal optimization of cathode/SE interface in ASSLBs (Figure S2b, Supporting Information).

In the intrinsic structure of layered oxides, the local atomic coordination surrounding oxygen is comprised of three linear Li–O–TM configurations.[22] Within such a configuration, oxygen electrons exhibit a higher propensity for extraction when compared to the TM–O–TM configuration commonly found in metal oxides. As a result, they display a preference for engagement in chemical redox reactions.[23,24] The surface nonstoichiometric or coordination loss configurations (such as under-coordinated oxygen ions on the edge planes, polar structure on the $LiCoO_2$ (LCO) surface, and Ni surface segregation on the NMC111 surface) would further enhance the activity for interface reaction.[22,25] Residual hydroxyl and carbonate can be formed on the surface of the layered cathode from its reaction with water and carbon dioxide in ambient air, which benefits dense coating as well as enhanced ionic conductivity.[26,27] Therefore, a proper in situ surface reconstruction that reduces surface activity for interface reaction through metal oxide passivation could be an effective strategy to build a stable and dense coating layer on the cathode material, which simplifies the preparation procedure without the introduction of the thin interface layer in ASSLBs.[22]

Motivated by the considerations outlined above, we present a strategy based on a gas–solid interface reduction reaction (GSIRR) involving layered oxides and a reducing gas (such as H_2, CO, and H_2S gas) to enable the in situ formation of a TMO/Li_2CO_3 layer on the CAM's surface. The schematic depiction of the GSIRR process, illustrating the interaction between layered oxides and reducing gas, is displayed in **Figure 1**a, while the detailed procedure can be found in the Experimental

Section. For LCO cathode, after the GSIRR process, a uniform CoO/Li_2CO_3 surface reconstructed layer (SRL) is constructed on the LCO particles, with a mere thickness of approximately 3–5 nm. The lattice structure undergoes a seamless transition from the layered LCO to the rock-salt CoO coating layer, signifying the phase transition from LCO to CoO. This reconstructed surface on the LCO cathode (referred to as SR-LCO) exhibits a remarkable initial discharge capacity of 149.7 mAh g^{-1} with obviously reduced polarization and capacity retention of 84.63% after 400 cycles at 0.2 C. Consequently, the SR-LCO cathodes, possessing elevated areal loadings (23.45 and 28.97 mg cm^{-2}), demonstrate exceptional electrochemical performance. They exhibit substantial specific capacities of 106.3 and 111.7 mAh g^{-1}, accommodating high current densities (0.5 and 0.3 C), and showcase exceptional cycling stability, enduring 250 and 150 cycles, respectively. This GSIRR method's superior performance, particularly when dealing with high loadings, surpasses that of most others, effortlessly satisfying the prerequisites for practical application (as summarized in Table S1, Supporting Information). The achievement of ultrahigh cathode areal loadings and remarkable electrochemical performance simultaneously is almost impossible to get in ASSLBs. Most importantly, this strategy has been extended to other reducing gases (H_2S and CO) and NCM811 cathode material. As confirmed by both experimental characterization and theoretical calculations, we attribute the improved electrochemical performance to a more stable (or less active) TMO phase, which can better stabilize sulfide-SE with fewer side reactions.

2. Results and Discussion

2.1. Phase Composition and Structure of LCO After GSIRR Process

SR-LCO samples were synthesized through the GSIRR process within a hydrogen (H_2) reductant atmosphere. The notation SR-LCO-X min (where X represents processing time of 5, 10, 15, and 20 min) distinguishes the samples resulting from varying GSIRR durations. X-ray diffraction (XRD) analysis (Figure 1b) coupled with "Rietveld" refinement (Figure S4, Supporting Information) reveals negligible disparities between the pristine LCO (P-LCO) and SR-LCO, barring the emergence of novel peaks at approximately 36.5°, 42.5°, and 61.6°, corresponding to the CoO phase (JCPDS No. 70–2856). These diffraction peaks' intensity progressively amplifies with prolonged reaction time. The Rietveld refinement shows that SR-LCO-10 min exhibits 1.68 wt% CoO (0.89 wt% for SR-LCO-5 min, 3.01 wt% for SR-LCO-15 min, and 7.62 wt% for SR-LCO-20 min) (Figure 1c). Remarkably, the lattice parameters display negligible variation after treatment, affirming the preservation of LCO's bulk crystal structure (Figure S5, Supporting Information). For visual insight, scanning electron microscopy (SEM) images in Figures S6,S7 (Supporting Information) depict the morphology of P-LCO and SR-LCO-10 min particles. Both P-LCO and SR-LCO particles exhibit well-crystallized structures and smooth surfaces, with a particle diameter ranging from 4 to 5 μm.

The surface composition analysis of SR-LCO-10 min was further examined using spectroscopic techniques. As illustrated in **Figure 2**a–d, depth-profiling X-ray photoelectron spectroscopy (XPS) was employed to investigate the Co 2*p* and C 1*s* core spectra at different etching depth (0, 15, and 30 nm). Notably, the intensity of binding energy at 782.0/797.1 eV corresponding to bivalent cobalt (Co^{2+}), was found to be markedly higher in SR-LCO compared to P-LCO.[17,28] This Co^{2+} content in SR-LCO was consistently greater than that observed in P-LCO across all etching depths, emphasizing its significance. For C 1*s* core peaks, the same carbon-based species are observed for both specimens: C–C/C–H groups 284.8 eV, C=O groups 286.5 eV and C–O–C 289.0 eV. It is preferred to fit this region of the C 1*s* spectra with a single large peak (FWHM 4.0 eV) that accounts for several C–O groups that may be present within the surface, such as C–O–C, RO–CO_2Li, and $LiHCO_3$. Furthermore, a distinctive photoelectron peak was identified at 290 eV in SR-LCO, indicating the presence of carbonate (–CO_3). This stands in sharp contrast to P-LCO.[29,30] The differentiation between the two materials (SR-LCO and P-LCO) is elucidated in Figure 2e, which shows the Co X-ray absorption near edge structure (XANES) and extended X-ray absorption fine structure (EXAFS) of P-LCO and SR-LCO-10 min. Notably, in the total electron yield (TEY) mode, a 2.0 eV energy shift toward lower values was observed in the Co K-edge threshold photon energy position for SR-LCO-10 min, signifying a reduction in Co valence following GSIRR.[31,32] Comparative analysis of Co R-space spectra from Co K-edge TEY of P-LCO and SR-LCO-10 min is depicted in Figure S8 (Supporting Information), revealing similar bond distances for SR-LCO-10 min and P-LCO (1.5 Å for Co–O and 2.4 Å for Co–Co). This similarity suggests that the GSIR process has limited impact on the bulk crystal structures of the P-LCO sample. Figure 2f and Figure S9 (Supporting Information) present the O K-edge XANES spectra of P-LCO and SR-LCO-10 min in TEY and total fluorescence yield (TFY) modes, respectively. A distinctive feature around ≈534 eV (indicated by the red dashed line in Figure 2f) was exclusively observed on the surface of SR-LCO-10 min, attributed to carbonate formation.[30] This feature was notably absent in the P-LCO sample within a similar energy range. Intriguingly, the carbonate feature at ≈534 eV exhibited a weaker signal in the fluorescence yield (FY) mode (as shown by the red dashed line in Figure S10, Supporting Information), underscoring its prevalence primarily in the surface layer. Verification of –CO_3 presence on the SR-LCO surface was further confirmed through Fourier-transform infrared spectroscopy (FTIR) analysis (Figure S11, Supporting Information). To explore the electrochemical behavior, differential electrochemical mass spectrometry (DEMS) experiments were conducted on SR-LCO during cell charging (Figure S12, Supporting Information). The signals indicated the decomposition of Li_2CO_3, with CO_2 evolution; however, the signal for CO_2 was relatively modest, indicating the limited presence of amorphous Li_2CO_3 in SR-LCO-10 min.

To understand the nature of the surface layer, high-resolution transmission electron microscopy (HRTEM) measurements were conducted on LCO before and after the GSIRR process (**Figure 3**a). Before the TEM observation, SR-LCO-10 min particles were sliced into a thin flake by focused ion beam (FIB) technology (Figure S13, Supporting Information). In the TEM image of the particle cross-section (after FIB) of Figure 3a, we note two different lattice fringes on SR-LCO-10 min, labeled as regions A and B. Fast Fourier transform (FFT) of region A is indexed to [100] zone of LCO phase (Figure 3b), while FFT of region B is

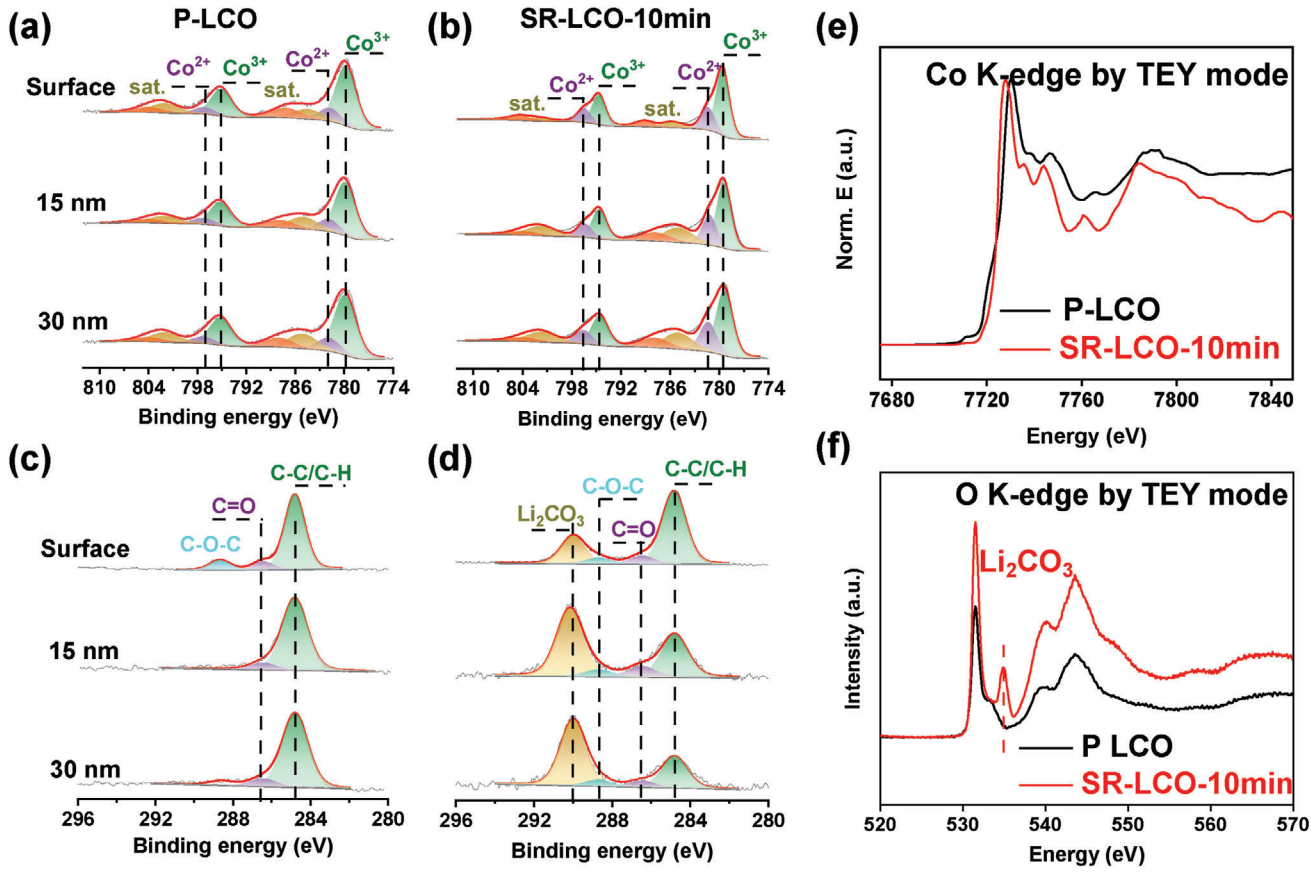

Figure 2. Surface characterizations of X-ray photoelectron spectroscopy (XPS) and X-ray absorption spectroscopy (XAS). a–d) XPS spectra of Co and C for the pristine LCO (P-LCO) and SR-LCO-10 min samples at different depths. e,f) XAS of P-LCO and SR-LCO-10 min: Co K-edge in total electron yield (TEY) mode and O K-edge in TEY mode, respectively.

indexed to [011] zone of CoO phase (Figure 3c). And a lattice space $d_1 = 4.65$ Å can be indexed to (003) plane of layered LCO (JCPDS card No.70-2685), and $d_2 = 2.47$ Å can be indexed to the (1-11) plane of rock-salt CoO (JCPDS card No. 70-2685) (Figure 3d). No discernible phase boundary exists between the inner layered phase LCO and outer rock-salt phase CoO, highlighting the seamless lattice coherence between the LCO core and CoO shell. And the rock-salt CoO phase layer exhibits a thickness of from 3 to 5 nm. Thus, the surface of SR-LCO-10 min undergoes progressive reconstruction from an R-3m-layered structure to an Fm-3m rock-salt one. Given the pronounced $-CO_3$ peaks observed in XPS and X-ray absorption spectroscopy (XAS) and the extraction of Li atoms to compensate for the changes in the phase transition of LCO → CoO, we speculate that the Li_2CO_3 phase is formed on the surface of SR-LCO. No $-CO_3$ diffraction peaks in XRD suggest that the amorphous region in TEM (Figure S14, Supporting Information) is the Li_2CO_3 amorphous phase. Energy dispersive spectroscopy (EDS) mappings (Figure S15a–d, Supporting Information) under TEM accurately indicate that the Co and O signals gather on SR-LCO-10 min from surface to bulk, while a visual C signal is concentrated on the surface.

To gain deeper insights into the structural and valence transformations occurring within LCO during the GSIRR process, we conducted high-angle annular dark-field scanning transmission electron microscope (HAADF–STEM) imaging and electron energy loss spectroscopy (EELS) mapping (Figure 3e). The electron diffraction pattern of a single SR-LCO particle unmistakably reveals the presence of a rock-salt CoO phase, which manifests as a distinct layer approximately 3 nm in thickness (Figure 3f), which is consistent with that observed in Figure 3a. The lattice patterns of both the layered LCO and the rock-salt CoO (as indicated by the corresponding FFT patterns) are remarkably well-defined, accentuating the clear boundary demarcating these two phases. By employing multiple linear least squares (MLLS) fitting in EELS analysis, we observe in Figure 3g that Co^{2+} ions (highlighted in the green box) are homogeneously distributed across the particle's surface. In contrast, Co^{3+} ions (enclosed within the red box) exhibit an interior distribution. The spatial separation of these two valence states of cobalt is evident and sharply defined. The inset of Figure 3g provides additional validation, exhibiting the peak positions and energy shifts of Co signal. This further substantiates the coexistence of both Co^{2+} and Co^{3+} valence states subsequent to the GSIRR process. Encouragingly, the findings from the EELS analysis harmoniously align with those derived from XAS, corroborating the conclusion. In light of the congruent results obtained from XRD, XPS, XAS, and TEM investigations, we establish that the GSIRR approach seamlessly introduces a surface-reconstructed CoO/Li_2CO_3 layer with a thickness of

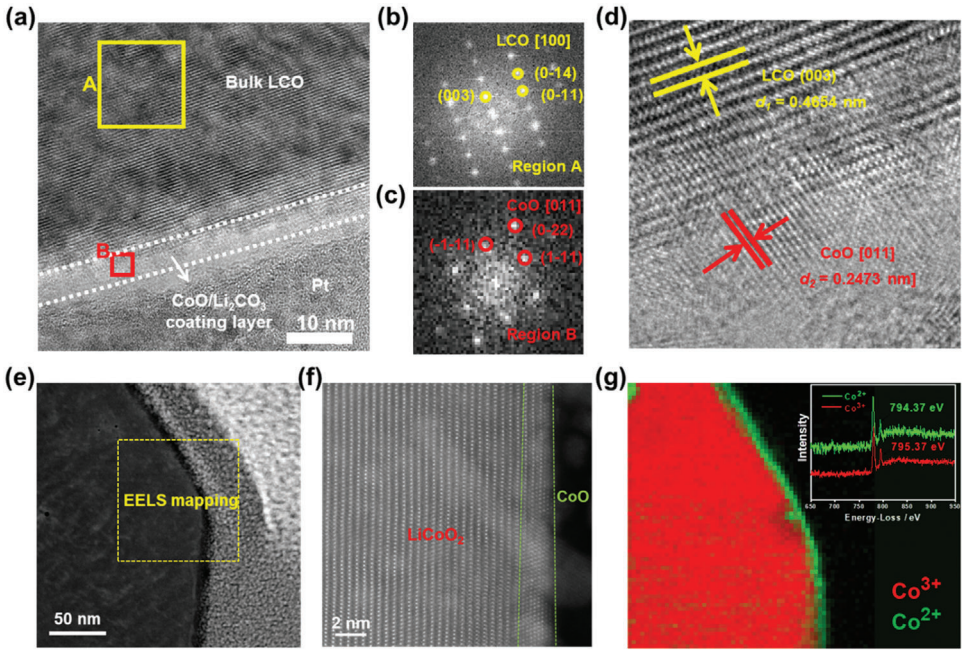

Figure 3. Scanning transmission electron microscope high-angle annular dark-field (STEM–HAADF) images and electron energy loss spectroscopy (EELS) analysis of SR-LCO materials. a) Transmission electron microscopy (TEM) image and corresponding fast Fourier transform (FFT) results for region A (b) and region B (c) of SR-LCO-10 min. d) High-resolution transmission electron microscopy (HRTEM) image of SR-LCO-10 min sample. e–g) HAADF–STEM images and EELS elemental mapping of Co2+ and Co3+. The yellow rectangle of the STEM image indicates the analysis area. The inset in Figure 3g is the high-resolution EELS profile of Co^{2+} and Co^{3+}.

approximately 3 to 5 nm. Notably, this introduction is accomplished without inducing any noticeable disruption to the bulk structure of the material.

2.2. Electrochemical Tests of P-LCO and SR-LCO

The electrochemical performance of the SR-LCO cathode was evaluated at various C-rates and room temperature within pelletized ASSLB cells, utilizing the Li-In alloy anode and LPSCl SE. A comparative analysis was conducted against the P-LCO cathode. **Figure 4**a,b depicts the cycling performance and rate capability of P-LCO and different SR-LCO variants (SR-LCO-X min where $X = 5$, 10, 15, and 20) at 0.2 and 0.5 C discharge rates, respectively. The cycling capacity results highlight SR-LCO-10 min as the most notable performer, delivering substantial capacity and retaining impressive rate capability even after hundreds of cycles. At 0.2 C, SR-LCO-10 min has a higher initial capacity of 135.5 mAh g^{-1} and improved capacity retention of 87.8% after 400 cycles, compared with an initial capacity of 99.0 mAh g^{-1} and rapid degradation upon cycling for the P-LCO. Similarly, at 0.5 C, SR-LCO-10 min maintains 81.7% capacity (135.2 mAh g^{-1}) after 300 cycles. Figures S16,S17 (Supporting Information) illustrate the 2nd charge–discharge curves of P-LCO and SR-LCO-X min at 0.2 and 0.5 C, respectively. Overall, SR-LCO-10 min exhibits reduced voltage polarization and enhanced capacity, indicating minimized interfacial resistances with sulfide SEs. In sharp contrast, P-LCO and SR-LCO-20 min exhibit significant polarization voltages and capacity deterioration. To reinforce the capacity performance of SR-LCO-10 min, Figure S18 (Supporting Information) presents its cycling stability with error bars. The rate capability analysis reinforces the superior capacity retention of SR-LCO-10 min compared to other cathodes (Figure 4c). SR-LCO-10 min can deliver >80% higher capacity at lower 0.1–0.5 C rates and more than 60% higher capacity at higher 1–2 C rates. Therefore, the SR-LCO with 10 min of thermal reduction stands out as the optimized candidate, consistently demonstrating the advantages of CoO/Li_2CO_3 SRL.

To better understand cycling performance associated with interfacial resistance in ASSLBs, a comprehensive set of electrochemical characterization techniques were employed on P-LCO and SR-LCO-10 min cathode materials. Specifically, cyclic voltammetry (CV), galvanostatic intermittent titration technique (GITT), and electrochemical impedance spectroscopy (EIS) measurements were conducted on cells of P-LCO and SR-LCO-10 min. The distinctive features of the initial capacity performance are clearly evident in the CV curves of both P-LCO and SR-LCO-10 min, as illustrated in Figure 4d and Figure S19 (Supporting Information). Notably, the current response and peak potential of oxidation and reduction processes in SR-LCO-10 min present noticeable changes when compared to those observed in P-LCO. This disparity is further emphasized by the narrower half-peak width, signifying a more favorable interfacial interaction between SR-LCO-10 min and LPSCl SE. The congruent trends are likewise reflected in the GITT profiles, as depicted in Figure S20a,b (Supporting Information). Remarkably, SR-LCO-10 min demonstrates diminished electrochemical polarization and enhanced reversibility during the discharge process. GITT results show that Li diffusion coefficient (D_{Li}) at SR-LCO-10 min is increased compared to P-LCO cathode, leading to increase in

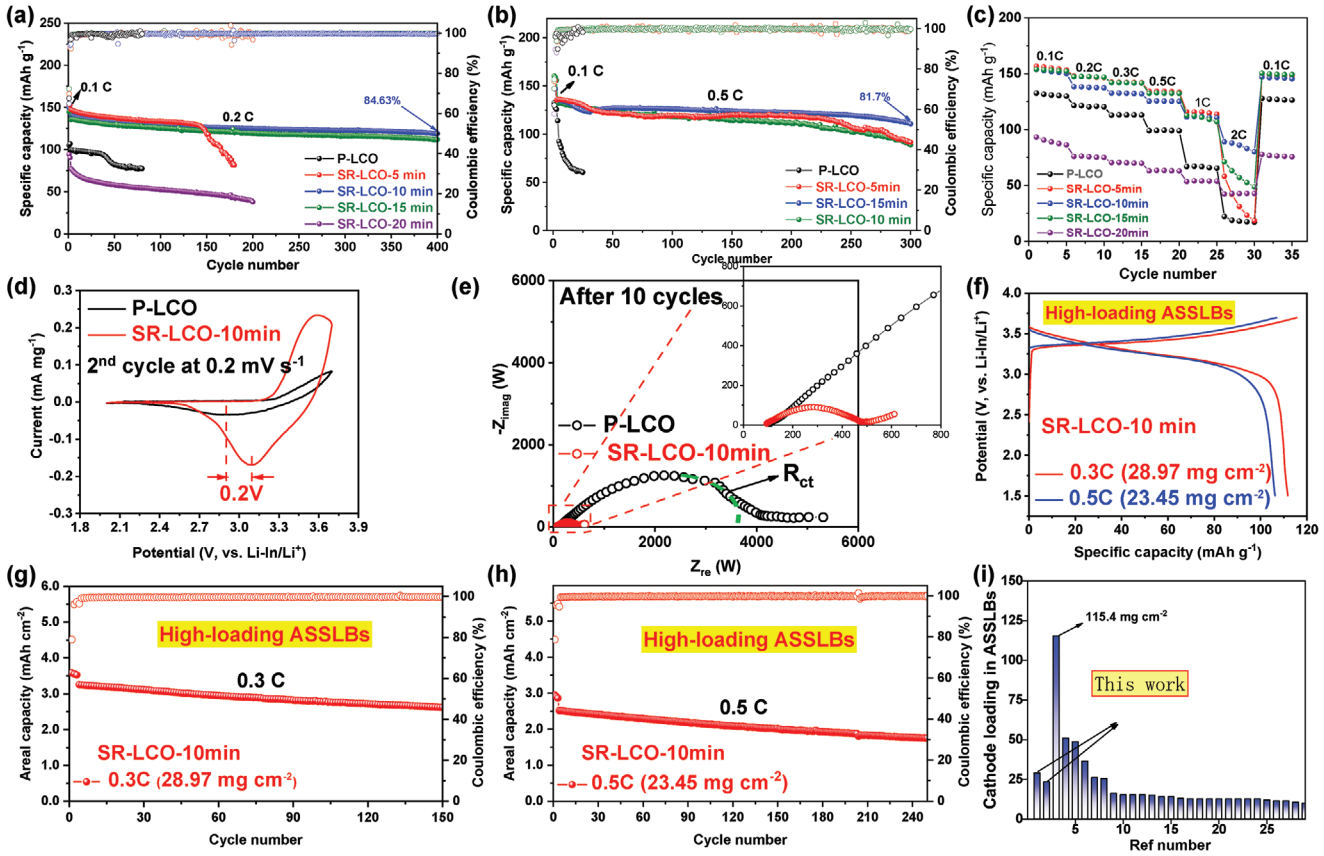

Figure 4. High-performance achieved with SR-LCO in all-solid-state lithium-ion batteries (ASSLBs). a,b) Long-term cycling stability of batteries employing pristine LCO (P-LCO) and SR-LCO-X min at 0.2 and 0.5 C rates, respectively. c) The rate capability of ASSLBs using P-LCO and SR-LCO-10 min, spanning rates from 0.1 to 2 C rates. Considering the rapid degradation observed in the P-LCO cathode, we conducted tests on more than five P-LCO ASSLB cells to identify a cell sustaining a rate above the 30th cycle under high C-rate conditions. d) The rate testing of batteries employing P-LCO and SR-LCO-X min at a scan rate of 0.2 mV s^{-1}. e) The Nyquist plots of ASSLBs with P-LCO and SR-LCO after 10 cycles at 0.2 C. f–h) SR-LCO-10 min ASSLBs with high loading, including the initial charge–discharge curves and the cycling performance at 0.3 and 0.5 C. i) The comparison of cathode areal loading in ASSLBs using the state-of-the-art ASSLBs reported in the literature. A more detailed comparison of electrochemical performance including cell design and operating conditions is shown in Table S1 (Supporting Information).

kinetics of electrochemical reactions and hence conduction of Li-ion. We calculated the ionic diffusion coefficient of the two cathode materials by the GITT and Equation 1. The Li-ion diffusion coefficient for SR-LCO-10 min (5.10×10^{-14} cm^2 s^{-1}) raises more than two orders of magnitude compared to P-LCO (1.68×10^{-16} cm^2 s^{-1}). Detailed EIS analyses coupled with the fitting of an equivalent circuit model using the transmission line concept (as shown in Figure 4e, Figures S21,S22 (Supporting Information), and Table S2, Supporting Information) provide additional insights. After 10 cycles, the P-LCO cell exhibits a significant increase in resistance,[33,34] with a high charge transfer resistance (R_{ct}) of 1532 Ω and a high resistance-capacitance (R_C) value of 318.5 Ω. These values unequivocally indicate a continuous deterioration of the LCO/LPSCl interface due to serious interface parasitic reactions (Table S3, Supporting Information). In contrast, the integration of CoO/Li_2CO_3 contributes significantly to the stability of the interface in the SR-LCO-10 min cathode. This is exemplified by the substantial reduction in the R_C parameter to 286.6 Ω and a significantly lower R_{ct} value of 118.7 Ω after 10 cycles. These outcomes strongly support the establishment of resilient solid–solid interfaces, even in the presence of intermittent physical contact at the solid–solid interfaces during cycling.

To comprehensively assess the cycling stability of SR-LCO-10 min cathode, we conducted ASSLBs with significantly elevated cathode loading, as depicted in Figure 4f–h. When subjected to a substantial loading of 28.97 mg cm^{-2} and operated at 0.3 C, the SR-LCO-10 min cathode exhibited an initial capacity of 111.7 mAh g^{-1} (equivalent to 3.24 mAh cm^{-2} areal capacity) and maintained a capacity of 94.95 mAh g^{-1} (equivalent to 2.76 mAh cm^{-2} areal capacity and 85% capacity retention) after 100 cycles (Figure 4g). Again, employing a higher loading of 23.45 mg cm^{-2} and operating at 0.5 C, the SR-LCO-10 min cathode delivered an initial capacity of 106.3 mAh g^{-1} (2.52 mAh cm^{-2} areal capacity) and exhibited a consistent capacity of 79.725 mAh g^{-1} (1.88 mAh cm^{-2} areal capacity and 75% capacity retention) after 200 cycles (Figure 4h). Notably, these areal capacity values surpass the threshold of 2.5 mAh cm^{-2}, a criterion deemed essential for fulfilling the demands of high energy density ASSLBs, thereby augmenting its practical uses. Figure 4i provides a visual comparison of the current cathode areal loading achieved in this work with that of the state-of-the-art ASSLBs reported in the existing

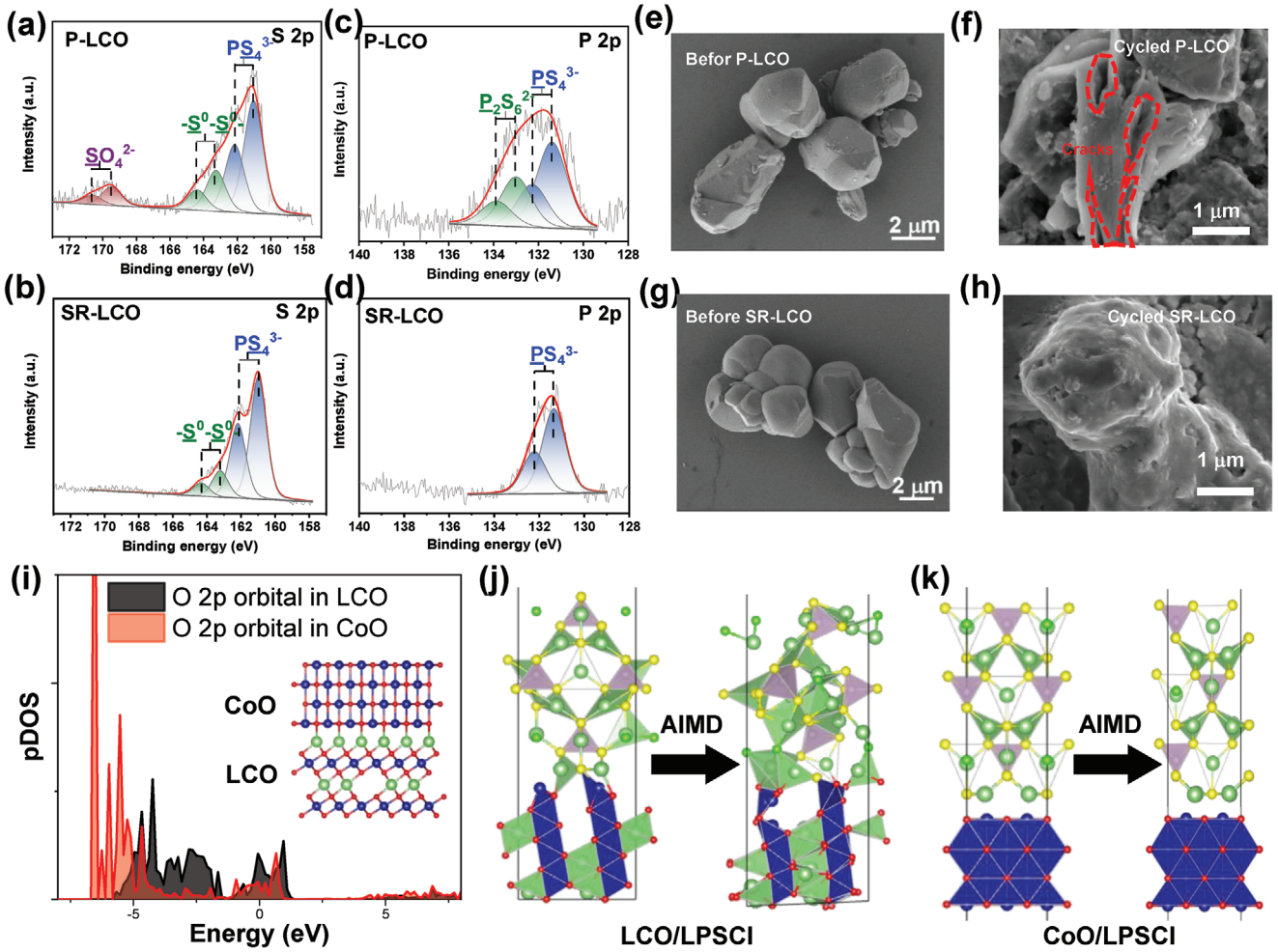

Figure 5. Revealing the interface stability with X-ray photoelectron spectroscopy (XPS), scanning electron microscopy (SEM), and density functional theory (DFT) calculations. a,b) S 2*p* and c,d) P 2*p* XPS spectra of pristine LCO (P-LCO)/LPSCl interface and SR-LCO-10 min/LPSCl interface after 10 cycles at 0.2 C. e–h) The SEM images of P-LCO and SR-LCO-10 min after 10 cycles at 0.2 C, respectively. i) Projected density of states (pDOS) of the O 2*p* orbitals of O atoms in layered LCO coordinated by two Li and three Co, and rock-salt CoO by six Co. Inset: atomic structure of LCO/CoO interface. j,k) The atomic structure of the LCO/LPSCl and CoO/LPSCl interface before and after 20 ps ab initio molecular dynamics (AIMD) simulation.

literature, with the distinctive data points for SR-LCO-10 min marked within a red box. For a more comprehensive assessment encompassing electrochemical performance, encompassing cell design and operational parameters, please refer to Table S1 (Supporting Information). The remarkable performance of SR-LCO-10 min is evident in its capability to accommodate high cathode areal loadings, coupled with proficient current density and robust cycling stability.

In addition, we also evaluated the electrochemical performance of both P-LCO and SR-LCO using liquid coin cells operating within the voltage range of 2.8–4.3 V (Li versus Li/Li^+). The charging/discharging voltage profile of SR-LCO-10 min shows a slight capacity reduction with no noticeable voltage polarization (Figure S23, Supporting Information). This observation suggests that CoO/Li_2CO_3 SRL as a proficient Li-ion conduction layer. Figure S24 (Supporting Information) displays the comparative rate capacity evaluation of P-LCO and SR-LCO across a range of rates from 0.2 to 5 C. The rate performance of SR-LCO-X min surpassed that of P-LCO, indicating remarkable improvements. Particularly noteworthy is the performance of the SR-LCO-15 min cathode, which demonstrated impressive capacities of 141.36, 114.93, and 62.85 mAh g^{-1} at 0.2, 2, and 5 C, respectively. Remarkably, even upon restoration to 0.2 C following discharge at 5 C, SR-LCO-15 min exhibited a sustained discharge capacity of 141.12 mAh g^{-1}. Thus, the enhanced cycling performance in liquid cells further proves the effectiveness of the GSIRR method on LCO cathode.

2.3. Discussion

It is natural to ask why the presence of CoO/L_2CO_3 SRL enhances the interfacial compatibility of LCO and LPSCl. To this end, we first analyzed the interphases in LCO/LPSCl sample after 10 cycles at 0.2 C by XPS measurement. Shown in **Figure 5**a–d are the XPS spectra of S 2*p* and P 2*p* core-level regions on the surface of two composite cathodes (P-LCO/LPSCl and SR-LCO/LPSCl). In the S 2*p* spectra (Figure 5a,b), there are three doublets of peaks

for P-LCO/LPSCl sample.[28,33,35–37] The rightmost doublet with peaks at binding energies of 161.0 ($2p_{3/2}$) and 162.3 eV ($2p_{1/2}$) corresponds to intrinsic PS_4^{3-} structural units in LPSCl and thus appears in both samples.[28,31,33,38] The middle doublet with peaks at binding energies of 163.3 ($2p_{3/2}$) and 164.4 eV ($2p_{1/2}$) corresponds to newly formed S–S bonds after cycling. The S–S bonds may belong to polysulfides and thiophosphate species (P_2S_x, x > 5). The leftmost doublet with peaks at binding energies of 169.5 ($2p_{3/2}$) and 170.7 eV ($2p_{1/2}$) corresponds to SO_4^{2-} structural units after cycling. It is important to note that the SO_4^{2-} peaks that existed in P-LCO/LPSCl significantly disappear in SR-LCO/LPSCl sample. Similar to P 2*p* data, there are two doublets of peaks after cycling in P-LCO/LPSCl sample. The lower binding energy doublet with peaks at binding energies of 131.4 ($2p_{3/2}$) and 132.3 eV ($2p_{1/2}$) corresponds to PS_4^{3-} structural units in LPSCl. The higher binding energy doublet with peaks at binding energies of 133.1 ($2p_{3/2}$) and 133.9 eV ($2p_{1/2}$) corresponds to newly-formed $P_2S_x^{2-}$ structural units in P-LCO/LPSCl sample. Again, the $P_2S_x^{2-}$ structural units disappear in SR-LCO/LPSCl sample. Taken together, XPS clearly demonstrates that the formation of SO_4^{2-} and $P_2S_x^{2-}$ related species is likely suppressed by CoO/Li_2CO_3 SRL in SR-LCO sample. What need reminds is, our XPS results are based on the surface of electrodes, etching a ≈10 μm thick layer from the electrode surface would result in a new doublet or an intensity increase, together with the appearance of other sulfur and phosphorus environments.

Next, we examined the surface morphologies of P-LCO and SR-LCO after cycling through postmortem scanning electron microscope (SEM) analyses. Figure 5e,f shows SEM images of P-LCO and SR-LCO-10 min electrodes after 10 cycles at 0.2 C. It can be seen that after 10 cycles, SR-LCO-10 min particles are wrapped with a mellow patina or slurry-like layer (Figure 5f), but P-LCO particles show visible microcracks and an exposed layer structure (circled in red), which suggests there is a degradation of the surface structure of the P-LCO particles (Figure 5e). The unstable and collapsed surface layer on P-LCO particles greatly reduces the utilization of active LCO materials after cycling. The SEM images of SR-LCO-10 min after 100 cycles were also studied. As shown in Figure S25a,b (Supporting Information), the LPSCl/Li-In interface structure and section of the Li-In anode preserve complete morphology with no any signs of mechanical cracking or contact loss after 100 cycles, which indicates the surface reaction between anode and solid electrolyte is not the main cause of battery failure.

To further interpret the influence of CoO/Li_2CO_3 layer on interface stability/reactivity, we performed the density functional theory (DFT) calculations from the following points of view: 1) whether or not the considered interface is thermodynamically stable in terms of phase equilibrium and oxygen reactivity calculations; and 2) when the considered interface is not thermodynamically stable, whether or not surface reaction, diffusion, and nucleation are the major kinetic factor. For the first point, the (electro)chemical stability of LPSCl and Li_2CO_3 was calculated. The DFT calculated electrochemical stability window of Li_2CO_3 overlaps with that of LPSCl. The thermodynamic oxidation limit of Li_2CO_3 is up to 4.2 V, close to the ASSLBs operating voltage window of 2.6–4.3 V versus Li^+/Li, indicating Li_2CO_3 is likely to remain stable over the entire ASSLBs cycling.

Then, the assessment of interfacial chemical stability was conducted through computations of chemical reaction energy, elucidating thermodynamic predisposition for reaction occurrence. We note that the chemical reaction energy of LCO-LPSCl (obtained from Equation 2) is considerably higher (–0.52 eV $atom^{-1}$) in comparison to Li_2CO_3-LPSCl (–0.13 eV $atom^{-1}$), implying a greater thermodynamic stability of Li_2CO_3 when in contact with LPSCl. At the interface of LCO and LPSCl, an oxidation process ensues within LPSCl, leading to the formation of phosphates, Li_2S, Co_3S_4, Li_2SO_4, and LiCl, while the oxygen ions within LCO partake in redox reactions. Considering the strong correlation between oxygen involvement and interface compatibility during cycling, the projected density of states (pDOS) of the oxygen 2*p* states of two oxygen environments (Co–O–Li configuration in LCO and Co–O–Co configuration in CoO) (Figure 5i). We found that the O 2p band center in rock-salt phase CoO is 2.75 eV lower than the O 2*p* band center of LCO. This indicates that Co–O–Co configuration in CoO shifts the depopulated O 2*p* states to lower energy and raises the O redox potential relative to that of the O redox in LCO by >2.75 V. We suggest that the strong Co–O–Co units of CoO play a vital role in suppressing interface side reaction at SR-LCO/LPSCl interface. For the second point, we simulated the ab initio molecular dynamics (AIMD) of the $LiCoO_2$/LPSCl and CoO/LPSCl interface to check the interface stability. We observed that the configuration degeneration (disordered CoO_x units and the formation of S–S bonds) at the $LiCoO_2$/LPSCl interface with AIMD simulation time becomes very obvious (Figure 5j,k). Surprisingly, at CoO/LPSCl interface, both CoO and LSPCl maintain a complete configuration structure with respect to AIMD simulation time, indicating CoO is kinetically stable toward LPSCl SE. From the findings described above, we may infer that CoO/LPSCl has better interfacial compatibility via the less reactivity of oxygen and higher kinetic passivation effect.

Based on the phase composition/structure analysis, electrochemical cell performance, and subsequent postprocessing XPS/SEM evaluations, we propose the presence of a synergy effect between Li_2CO_3 and CoO in mitigating parasitic reactions. The SRL layer significantly reduces interface resistance and enhances the interfacial stability of the cathode with sulfide SE. Within the SRL, CoO resides in the innermost layer, maintaining the crystal structural stability of LCO during the charge–discharge cycle. The amorphous Li_2CO_3 resides on the outer side of the layer, contributing to both ion conductivity and interface stability with sulfide electrolytes. Moremore, two additional factors contribute to the success of the CoO/Li_2CO_3 coating. Firstly, the CoO layer is exceptionally thin, measuring only ≈3 nm in thickness, thereby reducing the extent of the Li-ion diffusion pathway within the CoO layer. Secondly, we suggest that Li-ion diffusion through CoO coating belongs to the "space-charge model" and its transport is driven by an electric field. The CoO coating is electronically insulating, Li^+ is the only mobile species. No negative compensating charge exists in the CoO coating or the reduction of Co oxidation state, thus, a space charge develops in the CoO coating. Therefore, from the point, the dependency of the cell performance is not fully corresponded with H_2 exposure time or CoO thickness (Figure 4c). When H_2 exposure time is extended (Figure S26, Supporting Information), that is, the content of CoO is increased, potential adverse effects of CoO and particle aggregation could hinder the sustained

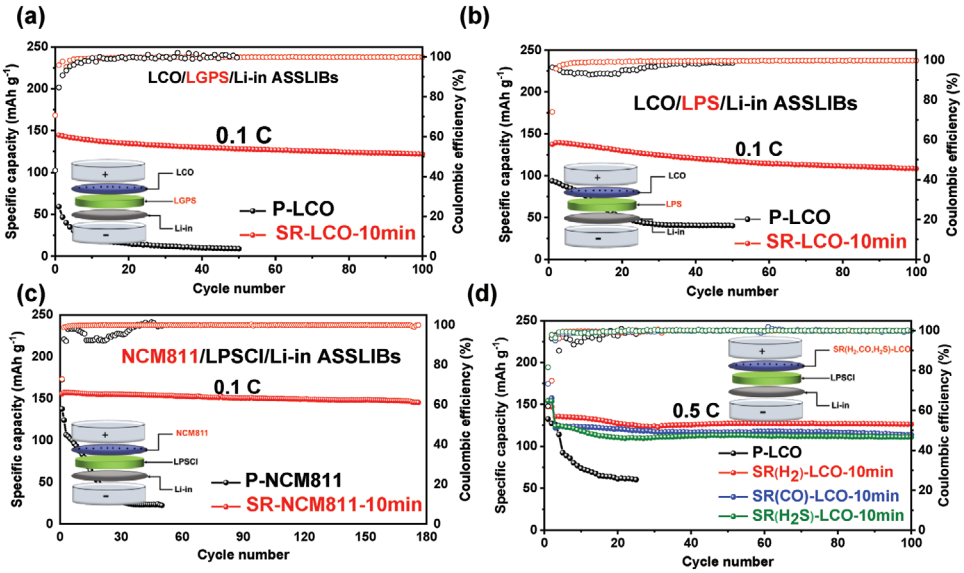

Figure 6. Generality and transferability. a,b) The cycling performance of all-solid-state lithium-ion batteries (ASSLBs) with pristine LCO (P-LCO) and SR-LCO-10 min using LGPS and LPS solid-electrolytes (SEs), respectively. c) The cycling performance of ASSLBs with NCM811 before and after gas–solid interface reduction reaction (GSIRR) process. d) The cycling performance of ASSLBs with LCO before and after treatment by various reducing gases (H_2, CO, and H_2S) at 0.5 C.

electrochemical performance of the SR-LCO in ASSLBs. Therefore, it is also important to choose an appropriate GSIRR process time, ensuring that the cathode material maintains optimal electrochemical performance.

2.4. Universality Investigation of GSIRR Method in ASSLBs

It is important to check whether SR-LCO has good interfacial compatibility with other sulfide SEs or not. We initiated our investigations by replacing the LPSCl SE with either LGPS or LPS sulfide SE in ASSLB cells. The cycling performance of LGPS-based ASSLBs is illustrated in **Figure 6**a. Remarkably, P-LCO displayed an initial capacity of 46.8 mAh g^{-1}, coupled with a steep deterioration over subsequent cycles and a notable charge/discharge voltage gap, as depicted in Figure S27a (Supporting Information). In sharp contrast, the SR-LCO configuration exhibited a robust initial discharge capacity of 143.6 mAh g^{-1} at a 0.1 C rate, accompanied by minimal overpotential. Its enduring cycling performance outshone expectations, with an impressive capacity retention of 85.90% after 100 cycles at 0.1 C (Figure 6a). Analyzing the S 2*p* XPS spectra of the LCO/LGPS interface post 10 cycles revealed that the cycled SR-LCO/LGPS interface exhibited no discernible peak intensity corresponding to CoS_x. Additionally, a reduction in the intensity of S species ($–S^0–S^0–$) was observed, in contrast to the cycled P-LCO/LGPS interface (Figure S27c,d, Supporting Information). Evident in Nyquist plots, the interface resistance of P-LCO ASSLB cells ballooned to over 40 000 Ω after 10 cycles, as depicted in Figure S27b (Supporting Information). Conversely, SR-LCO ASSLB cells demonstrated a significantly lower resistance with an R_c of 312.5 Ω and an R_{ct} of 260.4 Ω. Similarly, for LPS-based ASSLBs (Figure 6b), SR-LCO displayed a noteworthy first discharge capacity of 137.4 mAh g^{-1} at 0.1 C, maintaining an 80.0% capacity retention over the course of 100 cycles. The charge/discharge voltage gap was also minimal (Figure S28a, Supporting Information). Nyquist plots further elucidated the advantages of the cycled SR-LCO/LPS interface, which exhibited markedly lower resistance (≈200 Ω) compared to the cycled P-LCO/LPS interface (over 4000 Ω) (Figure S28b, Supporting Information). Thus, GSIRR-processed LCO exhibits good interfacial compatibility with LGPS and LPS sulfides SE.

It is also a challenge to achieve long-lasting NCM811-based ASSLB cells. GSIRR process was also employed to modify the surface of NCM811 to obtain a stable interface with LPSCl SE. XRD patterns suggest that NiO phase (JCPDS No. 47–1049) is created over the NCM811 surface (Figure S29a, Supporting Information). Because of the robust NiO phase, the SR-NCM811 (surface reconstructed NCM811) cathodes deliver 155.7 mAh g^{-1} first discharge capacity at 0.1 C, with 93.3% capacity retention up to 180 cycles. This ASSLB performance is in strong contrast to that of pristine NCM811 (P-NCM811), which just delivers a discharge capacity of 68.4 mAh g^{-1} at 0.1 C and preserves 49.4% capacity after 100 cycles (Figure 6c and Figure S29b, Supporting Information). Much smaller interfacial resistance after 10 cycles further supports the enhancement of interfacial stability (Figure S29c, Supporting Information). Moreover, the cycling performance of SR-NCM811with different cut-off voltages (from 3.8 to 3.9 and 4.0 V) (Figure S30, Supporting Information) shows that SR-NCM811 achieves a high capacity retentions of 71.73% after 160 cycles (2-3.9 V) and 75.20% after 115 cycles (2-4 V) at 0.2 C, respectively. Thus, the above results suggest that the GSIRR process also enhances the cycling stability of the NCM811 electrode by reengineering interfaces.

It should be pointed out that the other reducing gases may create a similar surface reconstructed layer. To further confirm the generality of the GSIRR method for oxide cathodes, we extended the H_2 gas to other reducing gas, including CO and H_2S. To

distinguish GSIRR processed LCO with different reducing gases (H_2, CO, and H_2S), SR-LCO-10 min is subdivided into SR(H_2)-LCO-10 min, SR(CO)-LCO-10 min, and SR(H_2S)-LCO-10 min, respectively. Figure 6d compares LCO/LPSCl/Li-In ASSLBs using the three different SR-LCO-10 min samples. After CO heat reduction, the same CoO/Li_2CO_3 SRL layer would be generated on the LCO surface (Figure S31a, Supporting Information), evidenced by pronounced CoO diffraction peaks in XRD pattern of SR(CO)-LCO-10 min. The thermal reduction by H_2S would also form the same SRL layer (Figure S31b, Supporting Information), indicating CoO/Li_2CO_3 SRL layer generation mainly contributes to the heat reduction of LCO no matter the type of reducing gases. After GSIRR process, SR(H_2)-LCO-10 min, SR(CO)-LCO-10 min, and SR(H_2S)-LCO-10 min can deliver similar initial capacities of 146.9, 153.7, and 157.8 mAh g^{-1} at 0.1 C, respectively. In contrast, P-LCO can only enable a reversible capacity of only 127.1 mAh g^{-1}, indicating an enhanced interface realized by GSIRR process. Besides that, efficient performance enhancement also can be demonstrated by the cycling stability at 0.5 C. Observably, high capacity retentions of 93.20%, 93.26%, and 91.13% after 100 cycles can be achieved by heat reduction by H_2, CO, and H_2S, respectively (Figure 6d). Relative chare–discharge curves at 0.1 and 0.5 C reveal smaller battery polarization after GSIRR process (Figure S32a,b, Supporting Information).

As for the reaction mechanism and the SRL change when using different reducing gases, we speculate the following mechanism: i) surface oxygen vacancies of CAM are created utilizing a reducing atmosphere and oxygen loss with flowing gas at high temperature, and ii) the surface structure of CAM transforms from layered to rock-salt phase by heat treatment. Different reducing gases would affect the kinetic rate of surface reaction and hence the thickness of surface phase transformation. In conclusion, the universality investigation of the GSIRR method figures out an efficient SRL layer fabrication by the GSIRR process, available in three sulfide-based SEs, providing a scale-up production method toward efficient interface stability improvement. Further studies along this line are needed to check whether GSIRR process will work for more cathode materials.

3. Conclusion

In summary, we have successfully implemented a straightforward yet highly effective method for surface reconstruction based on GSIRR. This approach was employed to create an in situ CoO/Li_2CO_3 SRL layer on the LCO cathode, yielding remarkable outcomes. The CoO/Li_2CO_3 SRL layer serves a dual purpose: firstly, it mitigates the adverse effects of high electronic energy levels from oxygen or oxidized oxygen species in the cathode, preventing any harm to the sulfide SE. Secondly, it establishes a conducive ion transport layer, effectively eliminating polarization issues. As a result of these advancements, the SR-LCO/LPSCL/Li-In ASSLB cells achieve excellent electrochemical performance, including higher initial discharge capacity, outstanding long cycling performance, much better rate performance, and lower resistance. Impressively, the cells maintain an impressive capacity retention rate of 85% even after undergoing 100 cycles at 0.3 C, all while boasting a high LCO areal loading of 28.97 mg cm^{-2}. Furthermore, we observed that other reducing gas, such as H_2S and CO, yield similar positive effects on the LCO cathode. Moreover, the CoO/Li_2CO_3 SRL layer applied to the LCO also plays a vital role in stabilizing the interface with LGPS and LPS. More importantly, the GSIRR process has been successfully extended to the in situ formation of NiO on NCM811, leading to enhanced cycling stability for NCM811. Our findings hold promise for the development of a range of transition metal oxides combined with Li_2CO_3, such as layered Ni-Mn-Co or Ni-Co-Al systems. This innovative approach could significantly enhance the compatibility of cathode/SE interfaces in all-solid-state lithium batteries in a cost-effective manner.

4. Experimental Section

Materials: Monocrystal $LiCoO_2$ and monocrystal $LiNi_{0.8}Co_{0.1}Mn_{0.1}O_2$ were provided by Xiamen Tungsten Co., Ltd (XTC). Indium foils (100 mm in thickness) were purchased from Canrd New Energy Technology Co., Ltd. SEs (Li_6PS_5Cl (LPSCl), b-Li_3PS_4 (LPS), $Li_{10}GeP_2S_{12}$ (LGPS)) were purchased from Hefei Kejing materials technology co., Ltd. Reducing gases (H_2, CO, H_2S) (8 Vol% with Ar as carrier gas) were provided by Guangzhou Dan Ou Dan Tong Trading Co. Lithium (99.99%, 50 mm in thickness) was brought from China Energy Lithium Co., Ltd.

Material Fabrication—Preparation of SR-LCO: P-LCO was conducted in a quartz tube furnace. To more precisely control the SRL layer over LCO, a multistep thermal procedure was applied. During the temperature increase, the N_2 flux was used as a protective gas. When the temperature rose to 650 °C, the gas was changed to H_2, and a reduction reaction between H_2 and LCO initiated. Following the cooling down process, the gas was changed to N_2 protection gas until reaching room temperature. Precise thickness control of SRL layer over LCO could be adjusted by limiting the holding time of H_2 flux. A series of SR-LCO oxides (denoted as SR-LCO-X min, X = 5, 10, 15, and 20 min) with different GSIRR reaction time with H_2 gas were obtained by controlling sintering time.

Preparation of SR(CO)-LCO and SR(H_2S)-LCO: The SR(CO)-LCO and SR(H_2S)-LCO were synthesized with a similar method to SR(H_2)-LCO by replacing the H_2 with CO or H_2S.

Preparation of SR-NCM811: SR-NCM811 was prepared by using a similar method to SR-LCO by replacing P-LCO with NCM811.

Electrochemical Tests—Cells Assembling: The cathode for ASSLBs was prepared by mixing the 150 mg cathode, 100 mg SEs, and 5 mg acetylene black by hand-milling for over 30 min. Then 10 mg cathode mixtures and 180 mg SEs were pressed into a pellet under 360 MPa (φ = 13 mm, with ≈4.5 mg cm^{-2} active material) for 10 min. An In foil and a Li foil were placed with cathode/SEs pellets followed by 20 MPa to assemble the ASSLBs. All the preparation processes of the ASSLBs mentioned above were carried out in an Ar-filled glovebox (H_2O/O_2 < 0.01 ppm).

Electrochemical Tests: The galvanostatic discharge/charge measurements of ASSLBs with LCO cathodes were conducted at a potential range of 2.6–4.3 V versus Li^+/Li using the battery tester system (LAND, Wuhan) under room temperature (25 °C), and 1 C was defined as 120 mA g^{-1}. For the ASSLBs with NCM811 cathodes, a potential range of 2.6–4.3 V versus Li^+/Li was applied, and 1 C was defined as 150 mA g^{-1}. The GITT curves of ASSLBs were performed with a 20 min discharge at 0.2 C followed by a 2-hrelaxation. The CV was used to investigate the electrochemical process of ASSLBs, performed at the CHI660E working station (Chenhua, Shanghai) at a voltage range of 2.6–4.3 V versus Li^+/L at a scan rate of 0.2 mV s^{-1}. The EIS of ASSLBs was performed in the Autolab working station (Wantong, Switzerland) with a frequency range from 105 to 0.01 Hz and an AC perturbation signal of 5 mV. Li^+ diffusion coefficient, D_{Li}, was calculated according to equation below:

$$D^{GITT} = \frac{4}{\pi\tau}\left(\frac{m_B V_M}{M_B S}\right)^2 \left(\frac{\Delta Es}{\Delta E\tau}\right)^2 \quad (1)$$

where τ is pulse duration time (1800 s); m_B is mass of LCO; M_B is the molecular weight of LCO (81.87 g mol^{-1}); V_m is the molar weight of LCO (32.13 cm^3 mol^{-1}); S is the area of the interfaces between LCO and sulfide SE: m_B times specific surface area of LCO (0.55 m^2 g^{-1}); ΔE_s represents the voltage difference between two consecutive steady states; ΔE_τ indicates the voltage change following a single pulse.

Materials Characterization: Powder X-ray diffraction (XRD) was carried out on Rigaku Ultima IV, the radiation source was Cu Kα, and the samples were scanned at a 2θ range of 5° to 90° with a scan speed of 1° min^{-1}. The XRD Rietveld refinement was performed in TOPAS software. A field emission scanning electron microscope (FESEM, Hitachi S-4800) was used to observe the morphologies of cathodes before and after reduction. FTIR (Nicolet 8700) was mainly used for the analysis of functional groups in LCO samples. The CoO/Li_2CO_3 SRL layer on the surface of LCO was observed via a high-resolution transmission electron microscope (HRTEM) at an accelerating voltage of about 200 kV. The SR-LCO-10 min samples were prepared by FIB. Electron energy loss spectroscopy was used in STEM to map the distribution of Co^{2+} and Co^{3+} in the samples. A PHI 5000 VB III electron spectrometer (XPS) was used to surface components of samples and cathode/SEs interface byproducts generation, and the binding energies reported herein were corrected regarding C–C/C–H signal at 284.8 eV. An Al Kα monochromatized radiation ($h\nu$ = 1486.6 eV) was employed as an X-ray source. The surface of the specimen is sputtered by inert gas ion bombardment with a sputter rate of 15 nm (SiO_2 as standard reference) for each time, and spectra are then collected from the center of an etched area. Survey spectra were recorded with a pass energy of 0.125 eV, and high-resolution spectra were recorded with a pass energy of 0.02 eV. Peak fitting was performed with the XPS Peak software. The local electronic environment of LCO cathode before and after treatment was determined by the X-ray absorption spectra at American light source (ALS). The obtained data were analyzed by Athena software. Co K-edge spectra were collected in total electron yield mode. O K-edge XANES spectra of LCO cathode were collected under the TEY and FY mode at spherical grating monochrometer (SGM) beamline.

Calculation Method: All DFT + U calculations were conducted using first-principles methodology within the Vienna ab initio simulation package (VASP), employing the projector augmented-wave approach.[39] The generalized gradient approximation (GGA) was used in the scheme of Perdew–Burke–Ernzerhof (PBE) to describe the exchange-correlation functional.[40,41] The plane-wave cutoff was set to 500 eV. The rotational invariant approach of Dudarev was used,[41] where a Coulomb parameter U and exchange parameter J are combined into a single U–J parameter. That is, this work referred to U instead of U–J. For 3d orbital of Co, the chosen value of U was 3.9 eV V in accordance with the previous theoretical study.[42] For LCO bulk structure, a 4 × 4 × 2 k-point grid was taken. For CoO and LPSCl bulk structures, a 4 × 4 × 4 k-point grid was taken. The interface chemical reactions were generated through the utilization of pymatgen. This process facilitated the identification of phase equilibria for targeted materials and chemical reactions.[43–45] For the cathode/SE interface, AIMD simulations were conducted. LCO/LPSCl interface and CoO/LPSCl interface structures were built considering the most stable surface of LCO and CoO surface. These AIMD simulations were grounded in the GGA–PBE functional, backed by a plane wave energy cutoff of 400 eV, and centered on a Gamma-only k-point sampling strategy. To capture the dynamics with precision, a time step of 2 fs was meticulously selected. The entire molecular dynamics process spanned a comprehensive temporal range of 20 ps, facilitating a comprehensive exploration of the system's behavior. The interface reaction energy of LCO and LSPCl was analyzed after computing the chemical reaction energy (ΔE) of LCO or LPSCl with respect to the possible reaction products. ΔE is defined as

$$\delta E\,(\mathrm{LCO} - \mathrm{LSPCl}) = E\,(\text{reaction products}) - E\,(\mathrm{LCO}) - E\,(\mathrm{LSPCl}) \quad (2)$$

The negative value of ΔE means the decomposition was favorable.

Supporting Information

Supporting Information is available from the Wiley Online Library or from the author.

Acknowledgements

This work was supported by the Province Natural Science Fund of Guangdong (2022A1515012476) and the National Natural Science Foundation of China (Projects 52150410411, 52172190 and 51874104).

Conflict of Interest

The authors declare no conflict of interest.

Author Contributions

Z.H. synthesized all the materials and conducted electrochemical measurements. B.Z. and Z.L. conceived the idea and designed the experiments. W.Z., Z.-W.Y., and M.Z. conducted XPS and TEM measurements. Z.Z. performed XAS analyses. B.Z., H.Z., S.Z., and Z.L. wrote the manuscript and all authors edited the manuscript.

Data Availability Statement

The data that support the findings of this study are available from the corresponding author upon reasonable request.

Keywords

all-solid-state, cathode, lithium-ion batteries, solid electrolyte, surface reconstruction

Received: June 14, 2023
Revised: September 23, 2023
Published online: December 7, 2023

[1] R. Chen, Q. Li, X. Yu, L. Chen, H. Li, *Chem. Rev.* **2020**, *120*, 6820.
[2] J. B. Goodenough, Y. Kim, *Chem. Mater.* **2010**, *22*, 587.
[3] Z. Lin, T. Liu, X. Ai, C. Liang, *Nat. Commun.* **2018**, *9*, 5262.
[4] S. Randau, D. A. Weber, O. Kötz, R. Koerver, P. Braun, A. Weber, E. Ivers-Tiffée, T. Adermann, J. Kulisch, W. G. Zeier, F. H. Richter, J. Janek, *Nat. Energy* **2020**, *5*, 259.
[5] Q. Zhang, D. Cao, Y. Ma, A. Natan, P. Aurora, H. Zhu, *Adv. Mater.* **2019**, *31*, 1901131.
[6] C. Yu, L. Van Eijck, S. Ganapathy, M. Wagemaker, *Electrochim. Acta* **2016**, *215*, 93.
[7] Y. Kato, S. Hori, R. Kanno, *Adv. Energy Mater.* **2020**, *10*, 2002153.
[8] B. Zhang, R. Tan, L. Yang, J. Zheng, K. Zhang, S. Mo, Z. Lin, F. Pan, *Energy Storage Mater.* **2018**, *10*, 139.
[9] N. Kamaya, K. Homma, Y. Yamakawa, M. Hirayama, R. Kanno, M. Yonemura, T. Kamiyama, Y. Kato, S. Hama, K. Kawamoto, A. Mitsui, *Nat. Mater.* **2011**, *10*, 682.
[10] Y. Kato, S. Hori, T. Saito, K. Suzuki, M. Hirayama, A. Mitsui, M. Yonemura, H. Iba, R. Kanno, *Nat. Energy* **2016**, *1*, 16030.
[11] W. D. Richards, L. J. Miara, Y. Wang, J. C. Kim, G. Ceder, *Chem. Mater.* **2016**, *28*, 266.

[12] H.-D. Lim, J.-H. Park, H.-J. Shin, J. Jeong, J. T. Kim, K.-W. Nam, H.-G. Jung, K. Y. Chung, *Energy Storage Mater.* **2020**, *25*, 224.
[13] Y. Yang, S. Wu, Y. Zhang, C. Liu, X. Wei, D. Luo, Z. Lin, *Chem. Eng. J.* **2021**, *406*, 126807 .
[14] C. Wu, J. Lou, J. Zhang, Z. Chen, A. Kakar, B. Emley, Q. Ai, H. Guo, Y. Liang, J. Lou, Y. Yao, Z. Fan, *Nano Energy* **2021**, *87*, 106081.
[15] Y. Xiao, Y. Wang, S.-H. Bo, J. C. Kim, L. J. Miara, G. Ceder, *Nat. Rev. Mater.* **2020**, *5*, 105.
[16] B. Zahiri, A. Patra, C. Kiggins, A. X. B. Yong, E. Ertekin, J. B. Cook, P. V. Braun, *Nat. Mater.* **2021**, *20*, 1392.
[17] S. H. Jung, K. Oh, Y. J. Nam, D. Y. Oh, P. Brüner, K. Kang, Y. S. Jung, *Chem. Mater.* **2018**, *30*, 8190.
[18] F. Walther, F. Strauss, X. Wu, B. Mogwitz, J. Hertle, J. Sann, M. Rohnke, T. Brezesinski, J. Janek, *Chem. Mater.* **2021**, *33*, 2110.
[19] Y. Seino, T. Ota, K. Takada, *J. Power Sources* **2011**, *196*, 6488.
[20] S. P. Culver, R. Koerver, W. G. Zeier, J. Janek, *Adv. Energy Mater.* **2019**, *9*, 1900626.
[21] U. Nisar, N. Muralidharan, R. Essehli, R. Amin, I. Belharouak, *Energy Storage Mater.* **2021**, *38*, 309.
[22] J. Chen, W. Deng, X. Gao, S. Yin, L.i Yang, H. Liu, G. Zou, H. Hou, X. Ji, *ACS Nano* **2021**, *15*, 6061.
[23] R. S. Negi, Y. Yusim, R. Pan, S. Ahmed, K. Volz, R. Takata, F. Schmidt, A. Henss, M. T. Elm, *Adv. Mater. Interfaces* **2022**, *9*, 2101428.
[24] C. Wang, L. Chen, H. Zhang, Y. Yang, F. Wang, F. Yin, G. Yang, *Electrochim. Acta* **2014**, *119*, 236.
[25] Z. Lu, G. Chen, Y. Li, H. Wang, J. Xie, L. Liao, C. Liu, Y. Liu, T. Wu, Y. Li, A. C. Luntz, M. Bajdich, Y. Cui, *J. Am. Chem. Soc.* **2017**, *139*, 6270.
[26] Y. You, H. Celio, J. Li, A. Dolocan, A. Manthiram, *Angew. Chem., Int. Ed.* **2018**, *57*, 6480.
[27] W. M. Seong, Y. Kim, A. Manthiram, *Chem. Mater.* **2020**, *32*, 9479.
[28] C.-W. Wang, F.-C. Ren, Y. Zhou, P.-F. Yan, X.-D. Zhou, S.-J. Zhang, W. Liu, W.-D. Zhang, M.-H. Zou, L.-Y. Zeng, X.-Y. Yao, L. Huang, J.-T. Li, S.-G. Sun, *Energy Environ. Sci.* **2021**, *14*, 437.
[29] Y. Bi, W. Yang, R. Du, J. Zhou, M. Liu, Y. Liu, D. Wang, *J. Power Sources* **2015**, *283*, 211.
[30] S. Deng, Q. Sun, M. Li, K. Adair, C. Yu, J. Li, W. Li, J. Fu, X. Li, R. Li, Y. Hu, N. Chen, H. Huang, L. Zhang, S. Zhao, S. Lu, X. Sun, *Energy Storage Mater.* **2021**, *35*, 661.
[31] S. Deng, X. Li, Z. Ren, W. Li, J. Luo, J. Liang, J. Liang, M. N. Banis, M. Li, Y. Zhao, X. Li, C. Wang, Y. Sun, Q. Sun, R. Li, Y. Hu, H. Huang, L. Zhang, S. Lu, J. Luo, X. Sun, *Energy Storage Mater.* **2020**, *27*, 117.
[32] J. Alvarado, C. Wei, D. Nordlund, T. Kroll, D. Sokaras, Y. Tian, Y. Liu, M. M. Doeff, *Mater. Today* **2020**, *35*, 87.
[33] J. Zhang, C. Zheng, L. Li, Y. Xia, H. Huang, Y. Gan, C. Liang, X. He, X. Tao, W. Zhang, *Adv. Energy Mater.* **2020**, *10*, 1903311.
[34] X. Li, Q. Sun, Z. Wang, D. Song, H. Zhang, X. Shi, C. Li, L. Zhang, L. Zhu, *J. Power Sources* **2020**, *456*, 227997,.
[35] R. Koerver, F. Walther, I. Aygün, J. Sann, C. Dietrich, W. G. Zeier, J. Janek, *J. Mater. Chem. A* **2017**, *5*, 22750.
[36] J. Auvergniot, A. Cassel, J.-B. Ledeuil, V. Viallet, V. Seznec, R. Dedryvère, *Chem. Mater.* **2017**, *29*, 3883.
[37] W. Zhang, F. H. Richter, S. P. Culver, T. Leichtweiss, J. G. Lozano, C. Dietrich, P. G. Bruce, W. G. Zeier, J. Janek, *ACS Appl. Mater. Interfaces* **2018**, *10*, 22226.
[38] C. Wang, X. Li, Y. Zhao, M. N. Banis, J. Liang, X. Li, Y. Sun, K. R. Adair, Q. Sun, Y. Liu, F. Zhao, S. Deng, X. Lin, R. Li, Y. Hu, T.-K. Sham, H. Huang, L. Zhang, R. Yang, S. Lu, X. Sun, *Small Methods* **2019**, *3*, 1900261.
[39] G. Kresse, J. Furthmüller, *Comput. Mater. Sci.* **1996**, *6*, 15.
[40] J. P. Perdew, K. Burke, M. Ernzerhof, *Phys. Rev. Lett.* **1996**, *77*, 3865.
[41] S. L. Dudarev, G. A. Botton, S. Y. Savrasov, C. J. Humphreys, A. P. Sutton, *Phys. Rev. B* **1998**, *57*, 1505.
[42] H. Yang, J.-Y. Yang, C. N. Savory, J. M. Skelton, B. J. Morgan, D. O. Scanlon, A. Walsh, *J. Phys. Chem. Lett.* **2019**, *10*, 5552.
[43] S. P. Ong, L. Wang, B. Kang, G. Ceder, *Chem. Mater.* **2008**, *20*, 1798.
[44] S. P. Ong, A. Jain, G. Hautier, B. Kang, G. Ceder, *Electrochem. Commun.* **2010**, *12*, 427.
[45] S. Wu, Y. Yang, C. Liu, T. Liu, Y. Zhang, B. Zhang, D. Luo, F. Pan, Z. Lin, *ACS Energy Lett.* **2021**, *6*, 290.